

EFFECT OF BEAM CHROMATICITY ON FOREGROUNDS IN WIDE-FIELD MEASUREMENTS OF REDSHIFTED 21 CM POWER SPECTRA

NITHYANANDAN THYAGARAJAN^{1*}, TBD

Draft version March 4, 2016

ABSTRACT

Keywords: cosmology: observations — dark ages, reionization, first stars — large-scale structure of universe — methods: statistical — radio continuum: galaxies — techniques: interferometric

1. INTRODUCTION

The period in the history of the Universe characterized by the transition of neutral hydrogen in the intergalactic medium (IGM) to a fully ionized state due to the formation of radiating objects such as the first stars and galaxies is referred to as the Epoch of Reionization (EoR). This is an important period of nonlinear growth of matter density perturbations and astrophysical evolution leading to the large scale structure observed currently in the Universe. And yet, this period in the Universe’s history has remained poorly probed to date with observations.

The redshifted neutral hydrogen from the IGM in this epoch has been identified to be one of the most promising and direct probes of the EoR (Sunyaev & Zeldovich 1972; Scott & Rees 1990; Madau et al. 1997; Tozzi et al. 2000; Iliev et al. 2002). Numerous experiments using low frequency radio telescopes targeting the redshifted 21 cm line from the spin-flip transition of HI have become operational such as the Murchison Widefield Array (MWA; Lonsdale et al. 2009; Bowman et al. 2013; Tingay et al. 2013), the Precision Array for Probing the Epoch of Reionization (PAPER; Parsons et al. 2010), the Low Frequency Array (LOFAR; van Haarlem et al. 2013) and the Giant Metrewave Radio Telescope EoR experiment (GMRT; Paciga et al. 2013). These instruments have sufficient sensitivity for a statistical detection of the EoR signal via estimating the spatial power spectrum of the redshifted HI temperature fluctuations (Beardsley et al. 2013; Thyagarajan et al. 2013). These instruments are intended to be precursors and pathfinders to the next generation of low frequency radio observatories such as the Hydrogen Epoch of Reionization Array³ (HERA; DeBoer et al. 2015) and the Square Kilometre Array⁴ (SKA). These next-generation instruments will advance the capability from a mere statistical detection of the signal to a direct three-dimensional tomographic imaging of the HI during the EoR.

The most significant challenge to low frequency EoR observations arises from the extremely bright Galactic and extragalactic foreground synchrotron emission which are $\sim 10^4$ times stronger than the desired EoR signal (Di Matteo et al. 2002; Ali et al. 2008; Bernardi et al. 2009, 2010; Ghosh et al. 2012). All the current and future

instruments rely on the inherent differences in spatial isotropy and spectral smoothness between the EoR signal and the foregrounds to extract the EoR power spectrum (see, e.g., Furlanetto & Briggs 2004; Morales & Hewitt 2004; Zaldarriaga et al. 2004; Santos et al. 2005; Furlanetto et al. 2006; McQuinn et al. 2006; Morales et al. 2006; Wang et al. 2006; Gleser et al. 2008).

When expressed in the coordinate system of power spectrum measurements described by the three-dimensional wavenumber (k), the foreground emission is restricted to a wedge-shaped region commonly referred to as the *foreground wedge* (Bowman et al. 2009; Liu et al. 2009, 2014a,b; Datta et al. 2010; Liu & Tegmark 2011; Ghosh et al. 2012; Morales et al. 2012; Parsons et al. 2012b; Trott et al. 2012; Vedantham et al. 2012; Dillon et al. 2013; Pober et al. 2013; Thyagarajan et al. 2013; Dillon et al. 2014) whereas the EoR signal has spherical symmetry due to its isotropy which appears elongated along line of sight k modes due to peculiar velocity effects when dominated by matter density perturbations during early stages of reionization.

The extreme dynamic range required to subtract foregrounds precisely demands high precision modeling of foregrounds as observed by modern wide-field instruments (Thyagarajan et al. 2015b,a). Their studies of effects of wide-field measurements of EoR power spectra have demonstrated the *pitchfork* effect wherein foreshortening of baselines causes a prominent enhancement of foreground power near the horizon limits of the *foreground wedge* as well in the contamination beyond. In this paper, we explore yet another phenomenon that inherently extends foreground power beyond the *wedge*, namely, that arising from the chromaticity of the antenna power pattern.

This paper is organized as follows. §2 introduces the HERA instrument. A brief summary of the delay spectrum technique used extensively in this analysis and the recently confirmed *pitchfork* effect are presented in §3. §4 describes foreground simulations including antenna beam pattern and all-sky foreground models. §5 investigates the effects of chromaticity of antenna beam on the resulting delay power spectrum and the cosmologically motivated constraints it places on dish reflectometry. Our findings are summarized in §7.

2. THE HYDROGEN EPOCH OF REIONIZATION ARRAY DeBoer et al.(2016)

3. DELAY SPECTRUM

¹ Arizona State University, School of Earth and Space Exploration, Tempe, AZ 85287, USA

* e-mail: t_nithyanandan@asu.edu

³ <http://reionization.org/>

⁴ <https://www.skatelescope.org/>

A brief description of the delay spectrum technique (Parsons et al. 2012a,b) is provided here. We borrow the notation used in Thyagarajan et al. (2015b).

Visibilities measured by an interferometer are given by (van Cittert 1934; Zernike 1938; Thompson et al. 2001):

$$V_b(f) = \iint_{\text{sky}} A(\hat{s}, f) I(\hat{s}, f) e^{-i2\pi f \frac{\mathbf{b} \cdot \hat{s}}{c}} d\Omega, \quad (1)$$

where, \mathbf{b} is the vector joining antenna pairs (commonly referred to as the baseline vector), \hat{s} is the unit vector denoting direction on the sky, f denotes frequency, c is the speed of light, $d\Omega$ is the solid angle element to which \hat{s} is the unit normal vector, $I(\hat{s}, f)$ and $A(\hat{s}, f)$ are the sky brightness and antenna's directional power pattern, respectively, as a function of \hat{s} and f . The *delay spectrum*, $\tilde{V}_b(\tau)$, is defined as the inverse Fourier transform of $V_b(f)$ along the frequency coordinate:

$$\tilde{V}_b(\tau) \equiv \int V_b(f) W(f) e^{i2\pi f \tau} df, \quad (2)$$

where, $W(f)$ is a spectral weighting function which can be chosen to control the quality of the delay spectrum (Vedantham et al. 2012; Thyagarajan et al. 2013), and τ represents the signal delay between antenna pairs:

$$\tau = \frac{\mathbf{b} \cdot \hat{s}}{c}. \quad (3)$$

The delay spectrum has a close resemblance to cosmological H I spatial power spectrum. Thus, the delay power spectrum is defined as:

$$P_d(\mathbf{k}_\perp, k_\parallel) \equiv |\tilde{V}_b(\tau)|^2 \left(\frac{1}{\Omega \Delta B} \right) \left(\frac{D^2 \Delta D}{\Delta B} \right) \left(\frac{\lambda^2}{2k_B} \right)^2, \quad (4)$$

with

$$\mathbf{k}_\perp \equiv \frac{2\pi(\frac{\mathbf{b}}{\lambda})}{D}, \quad (5)$$

$$k_\parallel \equiv \frac{2\pi\tau f_{21} H_0 E(z)}{c(1+z)^2}, \quad (6)$$

where, ΔB is the bandwidth, λ is the wavelength of the band center, k_B is the Boltzmann constant, f_{21} is the rest frame frequency of the 21 cm spin flip transition of H I, z is the redshift, $D \equiv D(z)$ is the transverse comoving distance, ΔD is the comoving depth along the line of sight corresponding to ΔB , and h , H_0 and $E(z) \equiv [\Omega_M(1+z)^3 + \Omega_k(1+z)^2 + \Omega_\Lambda]^{1/2}$ are standard terms in cosmology, and following Parsons et al. (2014),

$$\Omega \Delta B = \iiint |A(\hat{s}, f) W(f)|^2 d\Omega df. \quad (7)$$

We note that these visibilities and delay power spectra are dependent on right ascension (RA) of the pointing as well as the center of the frequency band. We defer expressing visibilities and delay power spectra explicitly as a function of pointing or center frequency (or redshift) to later sections where it is necessitated.

In this paper, we use $\Omega_M = 0.27$, $\Omega_\Lambda = 0.73$, $\Omega_K = 1 - \Omega_M - \Omega_\Lambda$, $H_0 = 100 \text{ km s}^{-1} \text{ Mpc}^{-1}$, and $P_d(\mathbf{k}_\perp, k_\parallel)$ is in units of $\text{K}^2 (h^{-1} \text{ Mpc})^3$.

It was recently discovered that in wide-field measurements diffuse foreground emission from wide off-axis angles appear enhanced in the delay spectrum near the edges of the *foreground wedge* even on wide antenna spacings (Thyagarajan et al. 2015b). Called the *pitchfork* effect, this arises due to severe foreshortening of baseline vectors towards the horizon along joining the antenna pairs thereby enhancing their sensitivity to large scale structures in these directions. Since delay spectrum maps directions on the sky to delay bins, the emission from large scales near the horizon appears enhanced in delay bins near the horizon limits of the *foreground wedge*. Since these delay modes lie adjacent to those considered sensitive to the EoR signal, they cause a significant contamination of line-of-sight modes critical for EoR signal detection. These findings were confirmed in MWA observations (Thyagarajan et al. 2015a).

It was also demonstrated in these studies that design of antenna power pattern, specifically its amplitude near the horizon, is an important tool in mitigating foreground contamination caused by these wide-field effects. A dish characterized by a nominal *Airy* pattern was found to mitigate this contamination by over four and two orders of magnitude relative to a dipole and a phased array of dipoles respectively. HERA has significantly based its antenna design principles on these findings in choosing its antenna geometry while paying close attention to the properties of the resulting antenna power pattern.

In this paper, we investigate the spectral properties of the proposed dish design through their effects on the resultant foreground delay power spectrum and the constraints they place on attenuation required to suppress reflections between the dish-receiver assembly and antenna pairs to within tolerable limits.

4. SIMULATIONS

We simulate wide-field visibilities for 19-element HERA from all-sky antenna power pattern and foreground models using the PRISim⁵ software package. The simulations cover 24 hr of observation in *drift* mode consisting of 80 accumulations spanning 1080 s each. The total bandwidth is 100 MHz centered on 150 MHz consisting of 256 channels with 390.625 kHz frequency resolution. Models of the antenna power pattern and foregrounds are described below.

4.1. Antenna Power Pattern

The High Frequency Structural Simulator (HFSS) was used to model the dish and its angular response used in this study. The HFSS model used prime focus optics with a 14 m faceted parabola with a spar f/D ratio of 0.32. The model has a 1 m central hole in the aluminum surface which is filled with a dielectric material similar to dry soil. The feed used a full PAPER dipole inside of a cylindrical backplane, the backplane is modeled as an aluminum surface. For the metal parts of the dipole, the discs were modeled as aluminum at the actual size, and the arms and terminals were modeled as copper. Dielectric stand-offs and supporting members were included.

⁵ The Precision Radio Interferometry Simulator (PRISim) is publicly available at <https://github.com/nithyanandan/PRISim>

For the calculations, one pair of arms was excited using a modal port. These models cover a frequency range of 100–200 MHz in intervals of 1 MHz. Refer to DeBoer et al. (2016) for a complete description of the dish model.

For reference, we use two other models for the antenna power pattern. The first is a nominal *Airy* pattern corresponding to a uniformly illuminated circular aperture of 14 m diameter and the second is an achromatic model where the response of the design at 150 MHz of the HFSS model described above was fixed as the hypothetical response at all frequencies covering the entire band. This frequency independent model will be used to isolate the effects of spectral structures in the antenna power pattern (or beam chromaticity) on foreground delay power spectra. Hereafter, we refer to these three beams as ‘simulated’, ‘*Airy*’ and ‘achromatic’ models.

In a related series of papers, Neben et al. (2016) discuss the agreement of these simulated antenna beam patterns with actual measurements and Ewall-Wice et al. (2016) model the reflections and return loss expected in the proposed antenna-receiver assembly. Our focus in this paper is to investigate chromaticity of antenna power patterns from the point of view of their impact on foreground contamination in delay power spectra.

4.2. Foreground Model

Our all-sky foreground model is the same as the one in Thyagarajan et al. (2015b). It consists of diffuse emission (de Oliveira-Costa et al. 2008) and point sources. The latter is obtained from a combination of the NRAO VLA Sky Survey (NVSS; Condon et al. 1998) at 1.4 GHz and the Sydney University Molonglo Sky Survey (SUMSS; Bock et al. 1999; Mauch et al. 2003) at 843 MHz with a mean spectral index of -0.83. The diffuse sky model has an angular resolution of 13.74 and a spectral index estimated for every pixel.

4.3. EoR Model

For reference, we use two models of EoR. In the first, simulations of the HI signal were created using the publicly available 21cmFAST⁶ code described in Mesinger et al. (2011). The code uses the excursion set formalism of Furlanetto et al. (2004) to generate ionization and 21cm brightness fields for numerous redshifts. The model shown in this paper assumes the same fiducial values of $T_{\text{vir}}^{\text{min}} = 2 \times 10^4$ K (virial temperature of minimum mass of dark matter halos that host ionizing sources), $\zeta = 20$ (ionization efficiency), and $R_{\text{mfp}} = 15$ Mpc (mean free path of UV photons) which predicts the redshift of 50% ionization (and hence a peak in the power spectrum signal) to be at $z = 8.5$ as in Ewall-Wice et al. (2016; submitted). The second model is borrowed from the simulations described in detail in Lidz et al. (2008). Hereafter, we refer to these two as EoR models 1 and 2 respectively.

5. CHROMATICITY OF POWER PATTERN

The equation for delay spectrum describes the mapping between sky location of a foreground object and delay. The chromatic nature (variation with frequency) of the antenna power pattern results in a convolution of

the geometrical mapping with the delay response of spectral chromaticity of the power pattern. This can result in a significant spillover of foreground power beyond the horizon delay limits especially in the case of foregrounds near the horizon.

5.1. Effect on Foreground Contamination

Since our aim in this paper is to quantify foreground contamination and EoR sensitivity without employing any sophisticated *foreground removal* techniques, we turn out attention to *foreground avoidance* strategy that employs spectral weighting technique. In such an estimation of power spectrum, specific choices for spectral weighting function, $W(f)$, have been found to be effective in reducing foreground contamination by many orders of magnitude (Thyagarajan et al. 2013) and is regularly used in EoR data analysis (Parsons et al. 2012a). For instance, a *Blackman-Harris* function (Harris 1978) has a dynamic range of $\sim 100 - 120$ dB in delay power spectrum and a reduced effective bandwidth, with:

$$\epsilon = \frac{1}{B} \int_{-B/2}^{+B/2} |W(f)|^2 df, \quad (8)$$

$$\text{and, } B_{\text{eff}} = \epsilon B, \quad (9)$$

where, $1 - \epsilon$ is the loss in overall spectral sensitivity and B_{eff} is the effective bandwidth. For a *Blackman-Harris* window function denoted by $W_{\text{BH}}(f)$, $\epsilon \approx 50\%$. Hence, the window spans a total of $2N$ frequency channels each of width Δf to have $B_{\text{eff}} \approx N \Delta f$.

Considering that the dynamic range required to suppress foreground contamination in the *EoR window* may probably be even higher than that provided by a *Blackman-Harris* window function, we use a modified version given by the convolution of a *Blackman-Harris* window with itself:

$$W(f) = W_{\text{BH}}(f) * W_{\text{BH}}(f). \quad (10)$$

In its Fourier domain, this window has a response that is obtained by squaring of the *Blackman-Harris* window response and thus improves the dynamic range further in the power response by another 100 – 120 dB while $\epsilon \approx 42\%$. This is an enormous gain in sidelobe characteristics for a negligible loss in over sensitivity relative to a simple *Blackman-Harris* weighting. This will ensure that the contamination resulting from spillover of foregrounds along the line-of-sight k -modes are limited by intrinsic spectral structures in the foregrounds and the beam patterns and not by sidelobes from spectral weighting. In this paper, we apply this modified spectral weighting function defined in equation 10 whenever foregrounds are represented in the Fourier delay domain.

In HERA-19 array layout, there are 30 unique baseline vectors and 8 unique baseline lengths. Fig. 2 shows the delay power spectra of foregrounds on the 8 unique baseline lengths obtained with the aforementioned models for power pattern at arbitrary local sidereal times (LST). In all these panels, the full-band spectrally weighted foreground delay power spectra obtained with achromatic, *Airy* and fully chromatic simulated beam patterns are shown in black, red, and blue respectively. The brightening of foreground power near the horizon limits (vertical dotted lines) due to the *pitchfork* effect

⁶ http://homepage.sns.it/mesinger/DexM_21cmFAST.html

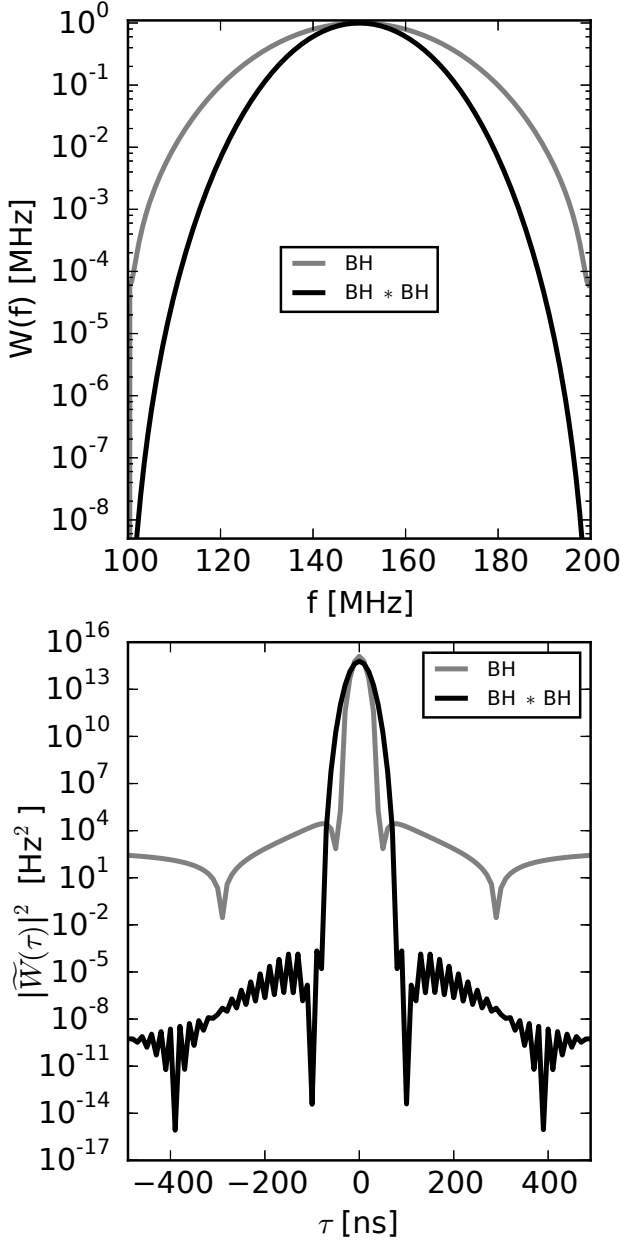


Figure 1. Choices for spectral weighting functions, $W(f)$ (top) and their delay power spectrum responses, $|\tilde{W}(\tau)|^2$ (bottom). The gray curves correspond to a *Blackman-Harris* window while those in black correspond to a *Blackman-Harris* window convolved with itself. The overall sensitivity of the former is $\epsilon \approx 50\%$ of a rectangular window while that of the latter is $\epsilon \approx 42\%$. Hence, the latter is narrower than the former. As a result, the main lobe of the convolved window function response is wider than that of a *Blackman-Harris* window. However, the sidelobes from the convolved window function are suppressed by more than ten orders of magnitude relative to that of a nominal *Blackman-Harris* window for only a slight loss of resolution.

(Thyagarajan et al. 2015b,a) is prominently seen in all cases. A clear trend of broadening of spillover-wings outside the horizon limits is seen with increasing chromaticity as the beam is changed from the achromatic to the *Airy* to the chromatic simulated model. For instance, the spillover from foreground delay power spectrum obtained with chromatic beam pattern is restricted

to $|k_{\parallel}| \lesssim 0.2 h \text{ Mpc}^{-1}$, with the *Airy* pattern it is restricted to $|k_{\parallel}| \lesssim 0.15 h \text{ Mpc}^{-1}$, while with the achromatic beam it is restricted to $|k_{\parallel}| \lesssim 0.12 h \text{ Mpc}^{-1}$ even on longest baseline lengths. It is also noted that despite the extreme dynamic range of the employed spectral weighting function, the tail of the foreground spillover at $|k_{\parallel}| \gtrsim 0.2 h \text{ Mpc}^{-1}$ with an *Airy* beam pattern is many orders of magnitude higher than that using an achromatic beam while that from the simulated chromatic beam is even higher than from an *Airy* pattern by a few orders of magnitude. This signals that the foreground spillover shown are truly limited by intrinsic spectral features in the antenna beam patterns.

It is clearly demonstrated that higher the beam chromaticity, the farther the foreground contamination inherently extends along k_{\parallel} . Thus, the chromaticity of antenna beam needs to be carefully controlled in EoR experiments in order to not allow sensitive k_{\parallel} -modes to become inaccessible for EoR HI signal detection.

It must be emphasized that such a significant spillover is not limited by the horizon limits of the *foreground wedge* because this is caused by spectral structure in the antenna beam pattern in addition to that caused by position-dependent geometric phase in the visibility spectra. As a result delay-based complex deconvolution techniques such as CLEAN (Taylor et al. 1999; Parsons & Backer 2009; Parsons et al. 2012b) that rely on smoothness of foreground spectra and only spectral window shape will not have adequate information to accurately deconvolve intrinsic supra-horizon spillover arising from the chromaticity of the antenna beam. We leave delay power spectrum estimation using *foreground removal* strategy that accounts for direction-dependent and beam chromaticity-dependent effects to future work and use only simple *foreground avoidance* approach in this study.

5.2. Constraints on Reflections in the Instrument

One of the primary causes for spectral structure in antenna power patterns is reflections in the instrument. Patra et al. 2015 (in preparation) and Ewall-Wice et al. (2016) discuss the measured and simulated reflections respectively between a dish and its feed. Reflection between structures and signal paths from different antennas also causes chromaticity in the antenna beam. In this section, we provide cosmologically motivated upper limits on instrument systematics caused by these two types of reflections.

The effect of reflections it to shift the measured foreground power to higher modes in τ (or equivalently in k_{\parallel}) and thus cause further contamination in these higher k_{\parallel} modes which are considered sensitive for EoR HI signal detection. Equivalently, these delay shifts introduce ripples in the spectrum. The net chromaticity in the measurements is the product of spectral structure arising out of the intrinsic nature of foreground emission, the baseline-dependent frequency structure of the fringes, the spectral features in the antenna power pattern besides any other spectral structures in the instrument unaccounted for. Equivalently, in the Fourier domain these factors have a convolving effect. In order to isolate the requirements on beam chromaticity from other sources of chromaticity, we start with an antenna beam in which those spectral structures are absent but the intrinsic

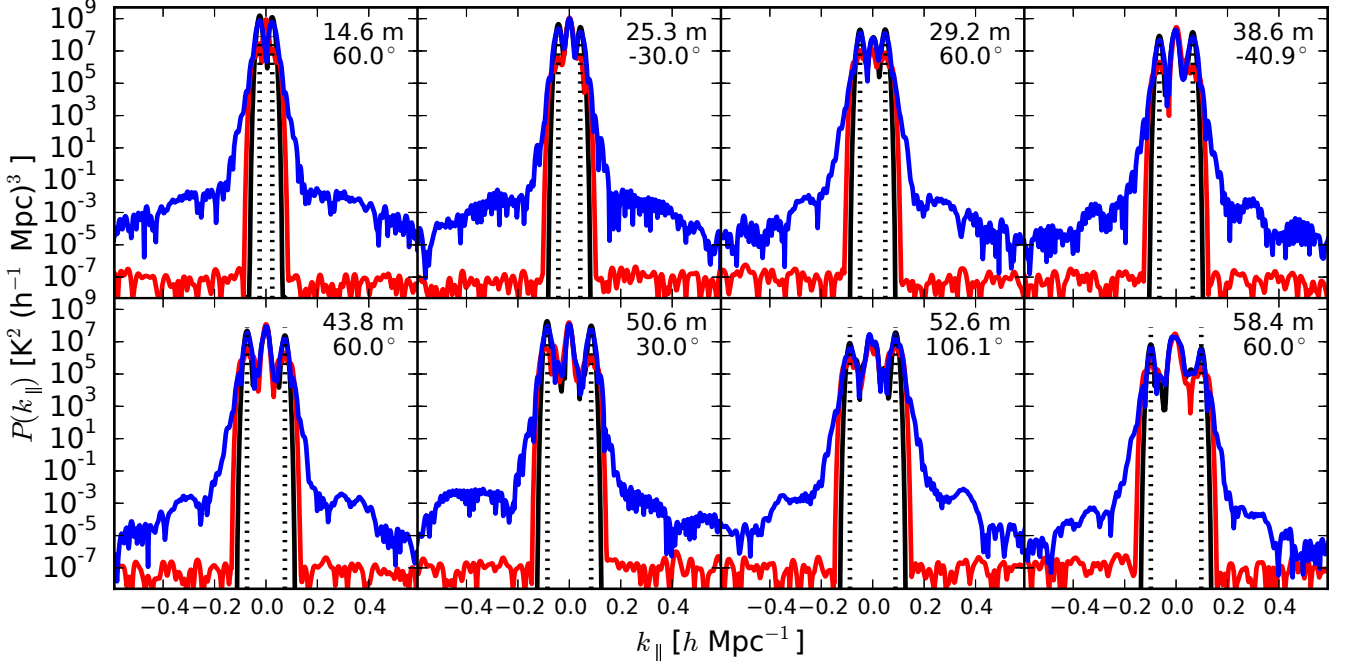


Figure 2. Foreground delay power spectra in units of $K^2(h^{-1} \text{ Mpc})^3$ on unique baseline lengths of HERA-19 at arbitrary LST. The baseline length and orientation (anti-clockwise from East) are annotated at the top right corner of each panel. Black, red and blue curves correspond to delay power spectra obtained with achromatic, *Airy* and chromatic simulated antenna beams respectively. The achromatic beam has no spectral structure, the simulated chromatic beam has maximum chromaticity while a nominal *Airy* pattern has intermediate level of chromaticity. The *pitchfork* effect is clearly visible as peaks around the horizon limits. With increase in chromaticity of the antenna beam the foreground spillover beyond the *foreground wedge* becomes progressively worse - the extent of foreground-spillover wings beyond the horizon limits (vertical dotted lines) and the amplitude of spillover beyond $k_{\parallel} \gtrsim 0.2 h \text{ Mpc}^{-1}$ is most severe for the chromatic simulated beam, intermediate for an *Airy* pattern and negligible for an achromatic beam.

sic chromaticity of foregrounds and the baseline fringes are included.

We define the required attenuation on the reflected foreground power as the ratio:

$$\Gamma_{k_p}(\tau) \geq \min_{|k_{\parallel}| > k_p} \left\{ \frac{P_{\text{FG}}(k_{\parallel} - \frac{dk_{\parallel}}{d\tau} \tau)}{P_{\text{HI}}(k_{\parallel})} \right\}^{1/2}, \quad (11)$$

where, $P_{\text{HI}}(k_{\parallel})$ is the EoR HI power spectrum for the chosen antenna spacing, $P_{\text{FG}}(k_{\parallel})$ is the foreground delay power spectrum obtained with the spectral weighting function applied over the full band of the three uniquely oriented 14.6 m antenna spacings further averaged over a 0–12 hr LST range and over both positive and negative k_{\parallel} modes, τ is the delay caused by reflections, and $dk_{\parallel}/d\tau$ is the *jacobian* in the transformation of τ to k_{\parallel} (see equation 6). Equivalently, $\Gamma_{k_p}(\tau)$ is determined by the requirement that the reflected foreground power obtained by shifting in delay is below the EoR HI signal power in line-of-sight spatial scales of interest given by $|k_{\parallel}| > k_p$. For this analysis constraining reflections, we use the 21cmFAST model at 150 MHz ($z \approx 8.47$) for $P_{\text{HI}}(k_{\parallel})$.

For reflections caused by dish-feed assembly, we use $P_{\text{FG}}(k_{\parallel})$ obtained with the achromatic beam model on a 14.6 m baseline in equation 11. Fig. 3 shows $\Gamma_{k_p}(\tau)$ (in dB) for k_p chosen to be $0.1 h \text{ Mpc}^{-1}$ (solid), $0.15 h \text{ Mpc}^{-1}$ (dashed), and $0.2 h \text{ Mpc}^{-1}$ (dotted). These curves set an upper limit to the reflected foreground power below the EoR HI signal power as a func-

tion of delays caused by dish-feed reflections. In other words, it implies that if reflections in the dish-feed assembly are attenuated to levels that lie in the regions below the different shaded regions, such spectral systematics in the instrument will not hinder detection of EoR in those corresponding k_{\parallel} modes of interest.

The elbow-shaped turnover is a measure of the most severe requirement on attenuation of reflections. This depends sensitively on the chosen k_{\parallel} modes. For instance, the attenuation required is $\gtrsim 54$ dB at ~ 200 ns for $k_p = 0.1 h \text{ Mpc}^{-1}$, $\gtrsim 56$ dB at ~ 300 ns for $k_p = 0.15 h \text{ Mpc}^{-1}$ and $\gtrsim 58$ dB at ~ 400 ns for $k_p = 0.2 h \text{ Mpc}^{-1}$. Measurements by Patra et al. (2016) for HERA dish-feed assembly show that the return losses lie well within the regions excluded by the shaded regions thus implying that the attenuation is well above the lower limit and hence will not prevent EoR detection.

Similarly, for reflections arising out of structures and interfaces across different antennas, we use $P_{\text{FG}}(k_{\parallel})$ obtained with the simulated chromatic and *Airy* antenna beams on 14.6 m baselines. These beams do not include spectral features from antenna-to-antenna reflections. Thus $\Gamma_{k_p}(\tau)$ provides lower limit for attenuation of antenna-to-antenna reflections. Fig. 4 is similar to Fig. 3 with constraints for values of k_p chosen to be $0.1 h \text{ Mpc}^{-1}$ (left), $0.15 h \text{ Mpc}^{-1}$ (middle), and $0.2 h \text{ Mpc}^{-1}$ (right). Lower limits are estimated for *Airy* (dashed lines) and simulated chromatic beams (solid lines).

Increase in beam chromaticity makes the lower limits on attenuating reflections more severe relative to that from an achromatic beam. For instance, for $k_p =$

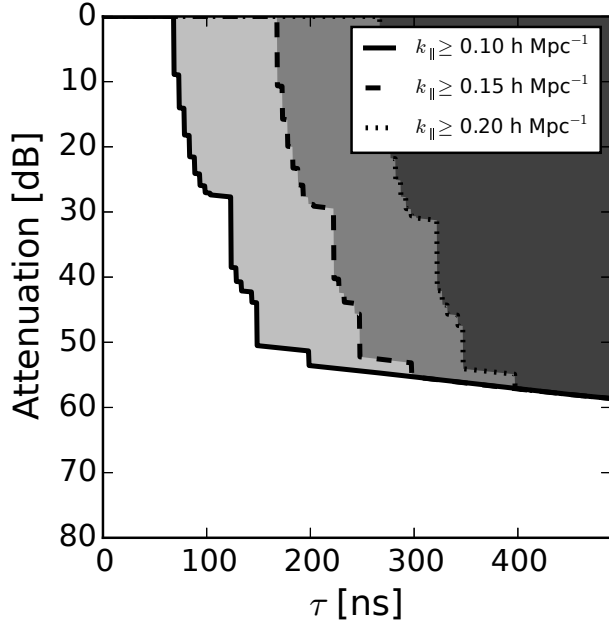


Figure 3. Lower limit on attenuation of reflected foreground power (in dB) from dish-feed reflections required to keep the reflected foreground power below EoR H_i signal power for all k_{\parallel} -modes greater than $0.1 h \text{ Mpc}^{-1}$ (solid), $0.15 h \text{ Mpc}^{-1}$ (dashed) and $0.2 h \text{ Mpc}^{-1}$ (dotted). This is obtained on 14.6 m antenna spacing for a 21cmFAST EoR model at 150 MHz ($z \approx 8.47$) and foreground power obtained with an achromatic antenna beam model. When the attenuation on dish-feed reflections is higher than these limits (outside the shaded regions), EoR will be detectable in respective k_{\parallel} -modes despite these reflections.

$0.1 h \text{ Mpc}^{-1}$ there is no delay at which the required attenuation is unconstrained to the left of the elbow-shaped turnover, including at $\tau = 0$. This means that when additional chromaticity from antenna-to-antenna reflections is taken into account, the requirement that all k_{\parallel} -modes with $k_{\parallel} > 0.1 h \text{ Mpc}^{-1}$ be accessible for EoR signal detection will not be satisfied with the currently simulated chromatic beam for HERA. For $k_p = 0.15 h \text{ Mpc}^{-1}$, there is a narrow range of allowed attenuation which is unconstrained for $\tau \lesssim 50$ ns. However, for $k_{\parallel} > 0.2 h \text{ Mpc}^{-1}$, the foreground power spectrum using simulated chromatic dish beam will have enough room to be effective for EoR signal detection despite additional chromaticity arising from antenna-to-antenna reflections.

It may be noted here that designing a dish whose antenna beam closely resembles a nominal *Airy* pattern will have a significantly higher ceiling of tolerance for allowing antenna-to-antenna reflections and yet remain very effective for EoR signal detection. The HERA collaboration is actively pursuing constant improvement of its dish design to keep minimize limitations from such chromatic systematics.

6. EOR SENSITIVITY

Here our goal is to estimate sensitivity for EoR detection in the presence of antenna beam chromaticity, using HERA as an example. As stated earlier, we estimate sensitivity of HERA in the most conservative scenario where we consider only *foreground avoidance* under simple spectral weighting scheme. We emphasize that other strategies involving *foreground removal* and inverse covariance-

based weighting schemes will produce more optimal results than presented here.

In order to avoid signal evolution across the entire bandwidth, we use subbands in which EoR signal evolution is not expected to be significant. These subbands with $B_{\text{eff}} = 10$ MHz are defined by spectral weights obtained by convolution of *Blackman-Harris* window with itself. These subbands are centered at 150 MHz and 170 MHz to estimate sensitivity at $z \approx 8.47$ and $z \approx 7.36$. We use independent EoR models 1 and 2 to reduce the dependence of this analysis on any single EoR model.

6.1. Sensitivity on Baseline- k_{\parallel} Parameter Space

We present the sensitivity of HERA against foregrounds obtained with three antenna beams of different chromaticities in two-dimensional parameter space of baseline lengths (transverse spatial scales) and k_{\parallel} (line-of-sight spatial scales). Fig. 5a and 5b show the EoR signal and foreground power in 150 MHz and 170 MHz subbands respectively. EoR models 1 and 2 are shown in cyan and gray respectively. The foreground delay power spectra obtained with achromatic, *Airy* and simulated chromatic antenna patterns are shown in black, red, and blue respectively. Each panel corresponds to a unique baseline vector, same as in Fig. 2.

Due to narrower subbands, the resolution of the foreground delay spectrum is coarser and the central region of foreground contamination extends to $|k_{\parallel}| \lesssim 0.2 h \text{ Mpc}^{-1}$. The coarsening of delay resolution significantly absorbs the distinct differences caused by beams of different chromaticities as seen in the full band foreground delay spectra outside the *foreground wedge* in Fig. 2. In other words, the foreground spillover wings that extend beyond the horizon even in the case of full-band simulated chromatic beam are on spectral scales larger than the 10 MHz effective bandwidth of the subbands. Hence, this results in an EoR signal-foreground crossover at $|k_{\parallel}| \gtrsim 0.2 h \text{ Mpc}^{-1}$ independent of different antenna beam chromaticities used in this analysis.

From Fig. 5, it is clearly demonstrated that HERA has significant sensitivity on all baselines in both subbands to detect EoR by more than two orders of magnitude above foreground contamination obtained with any level of antenna beam chromaticity. While this clearly includes foregrounds obtained with the currently simulated chromatic beam pattern, the sensitivity against foregrounds obtained with achromatic and *Airy* antenna power patterns are even higher by many orders of magnitude. This only further reiterates that efforts to keep lowering systematic spectral effects in the antenna beam must be undertaken continuously, as is the case with HERA.

6.2. Sensitivity on Baseline-RA Parameter Space

We investigate the EoR sensitivity in two dimensional parameter space formed by baselines and pointings in Right Ascension ($\text{RA} \equiv \alpha$) to highlight capabilities of HERA and provide clues for the best observing window.

In this section, we assume that the H_i power spectrum is isotropic (no sample variance) and hence, independent of α . However, it is dependent on the center of the subband, f_0 , where $f_0 = f_{21}/(1+z)$. The foreground delay power spectra depends on both f_0 and α . Thus, we rewrite the EoR H_i and foreground delay

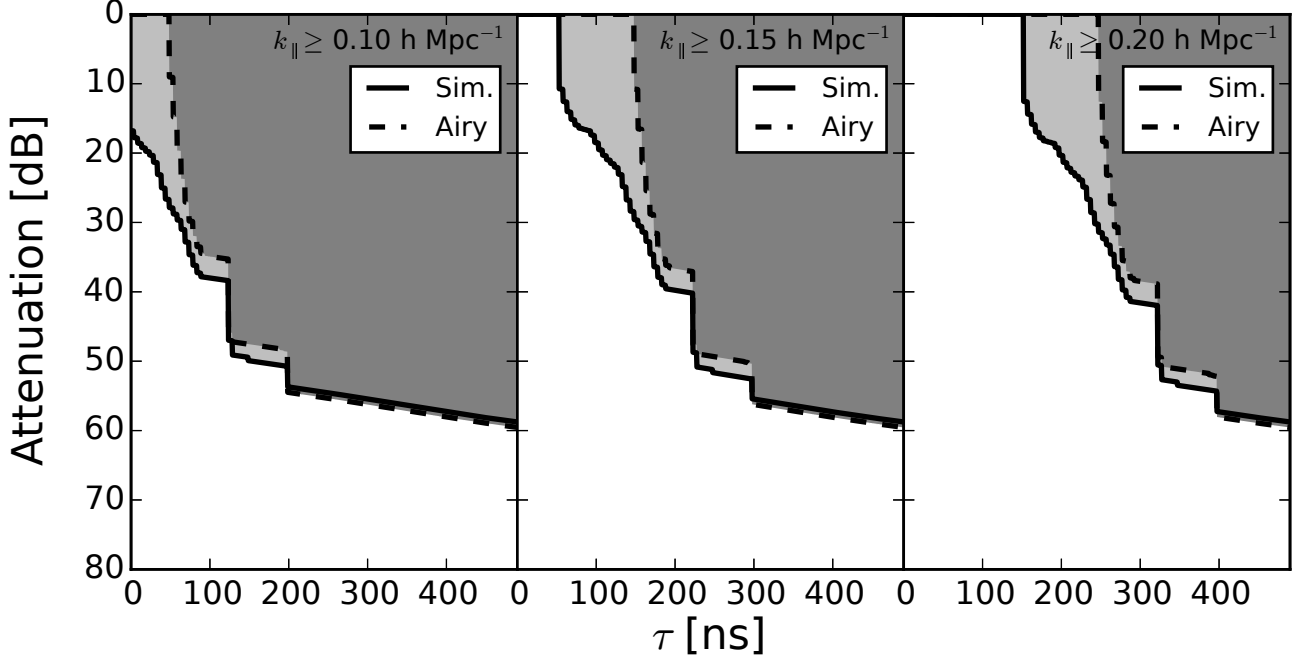


Figure 4. Lower limit on attenuation of reflected foreground power (in dB) from antenna-to-antenna reflections required to keep the reflected foreground power below EoR Hi signal power for all k_{\parallel} -modes greater than $0.1 h \text{ Mpc}^{-1}$ (left), $0.15 h \text{ Mpc}^{-1}$ (middle) and $0.2 h \text{ Mpc}^{-1}$ (right). This is obtained on 14.6 m antenna spacing for a 21cmFAST EoR model at 150 MHz ($z \approx 8.47$) and foreground power obtained with an *Airy* (dashed) and simulated chromatic (solid) antenna beam models. Regions excluding shaded regions indicate EoR will be detectable in respective k_{\parallel} -modes despite these reflections. Increase in beam chromaticity makes the requirement on attenuation more severe. For instance, $k_{\parallel} > 0.1 h \text{ Mpc}^{-1}$ modes will be inaccessible with the simulated chromatic beam if these reflections are taken into account. However, for the same beam the instrument will enjoy a much higher tolerance despite these reflections if the modes of interest are $k_{\parallel} > 0.2 h \text{ Mpc}^{-1}$ for EoR detection. Owing to lower chromaticity, an *Airy* beam offers higher tolerance to reflections compared to the simulated chromatic beam.

power spectra explicitly as a function of these quantities as $P_{\text{Hi}}(|\mathbf{b}|, k_{\parallel}, f_0)$ and $P_{\text{FG}}(\mathbf{b}, k_{\parallel}, f_0, \alpha)$ respectively.

We define baseline-dependent k_{\parallel} -modes of interest for *foreground avoidance* as $|k_{\parallel}| > k_{\parallel}^{\text{FA}}(\mathbf{b})$, with:

$$k_{\parallel}^{\text{FA}}(\mathbf{b}) = \frac{2\pi f_{21} H_0 E(z)}{c(1+z)^2} \left(\frac{|\mathbf{b}|}{c} + \frac{\zeta}{B_{\text{eff}}} \right), \quad (12)$$

where, the first term inside the parenthesis denotes the horizon limit, the second relates to the resolution due to subband bandwidth, B_{eff} , and ζ denotes a buffer to ensure $k_{\parallel}^{\text{FA}}(|\mathbf{b}|)$ threshold “avoids” the main lobe of foreground power.

We estimate the worst case sensitivity in the \mathbf{b} - α parameter space as:

$$\rho(\mathbf{b}, f_0, \alpha) = \min_{|k_{\parallel}| > k_{\parallel}^{\text{FA}}(|\mathbf{b}|)} \left\{ \frac{P_{\text{Hi}}(|\mathbf{b}|, k_{\parallel}, f_0)}{P_{\text{FG}}(\mathbf{b}, k_{\parallel}, f_0, \alpha)} \right\} \quad (13)$$

We consider the foreground power spectrum obtained with the simulated chromatic antenna beam, and EoR models 1 and 2, in each of the 150 MHz and 170 MHz subbands. Fig. 6 shows the worst case sensitivity, $\rho(\mathbf{b}, f_0, \alpha)$, for all 30 unique HERA baselines over 24 hours of α for the two EoR models and two subbands used in this study.

In general, sensitivity increases with longer baselines. We attribute this to the much steeper dependence of foreground emission on baseline length than that of EoR Hi power. This is also confirmed from Fig. 5 where the peak and sidelobe levels of foreground power obtained with the

simulated chromatic antenna beam on the 14.6 m baseline, which is sensitive to diffuse emission, progressively drops by two orders of magnitude on the 58.4 m baseline where diffuse emission is not as dominant. Hence, from a foreground contamination standpoint, the shortest baselines are less sensitive than the longer ones in the HERA-19 layout.

However, in all four cases considered here, the worst case signal-noise ratio lies above unity in most of this parameter space. It demonstrates that HERA will detect the EoR signal with a very high signal-noise ratio on all baselines in a vast majority of the pointings.

We reiterate that these estimates are obtained from a conservative scenario wherein only simple spectral weighting technique in the *foreground avoidance* limit is used, without any foreground removal or sophisticated weighting strategies using inverse-covariance. Further, these estimates represent worst-case lower limits demonstrating that HERA-19 and its successors will be extremely sensitive for EoR experiments and will benefit even further with more optimal foreground suppression strategies.

7. SUMMARY

This work was supported by the U. S. National Science Foundation (NSF) through award AST-1109257.

REFERENCES

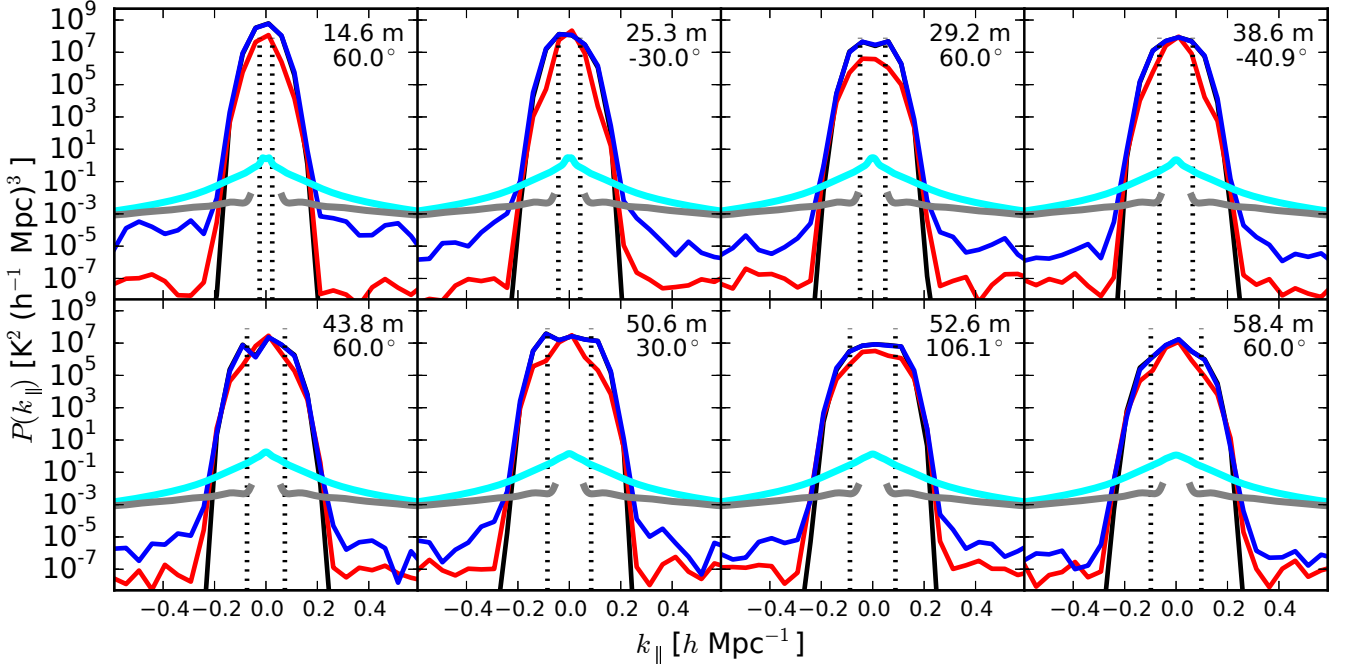
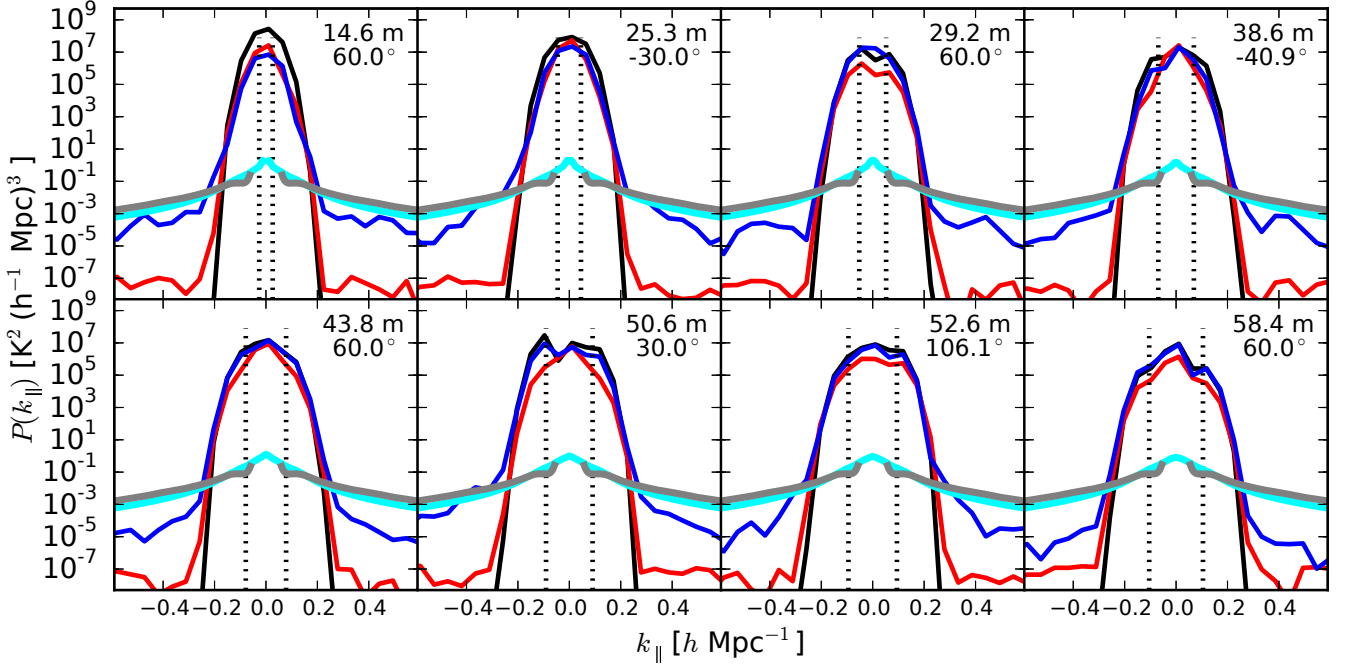
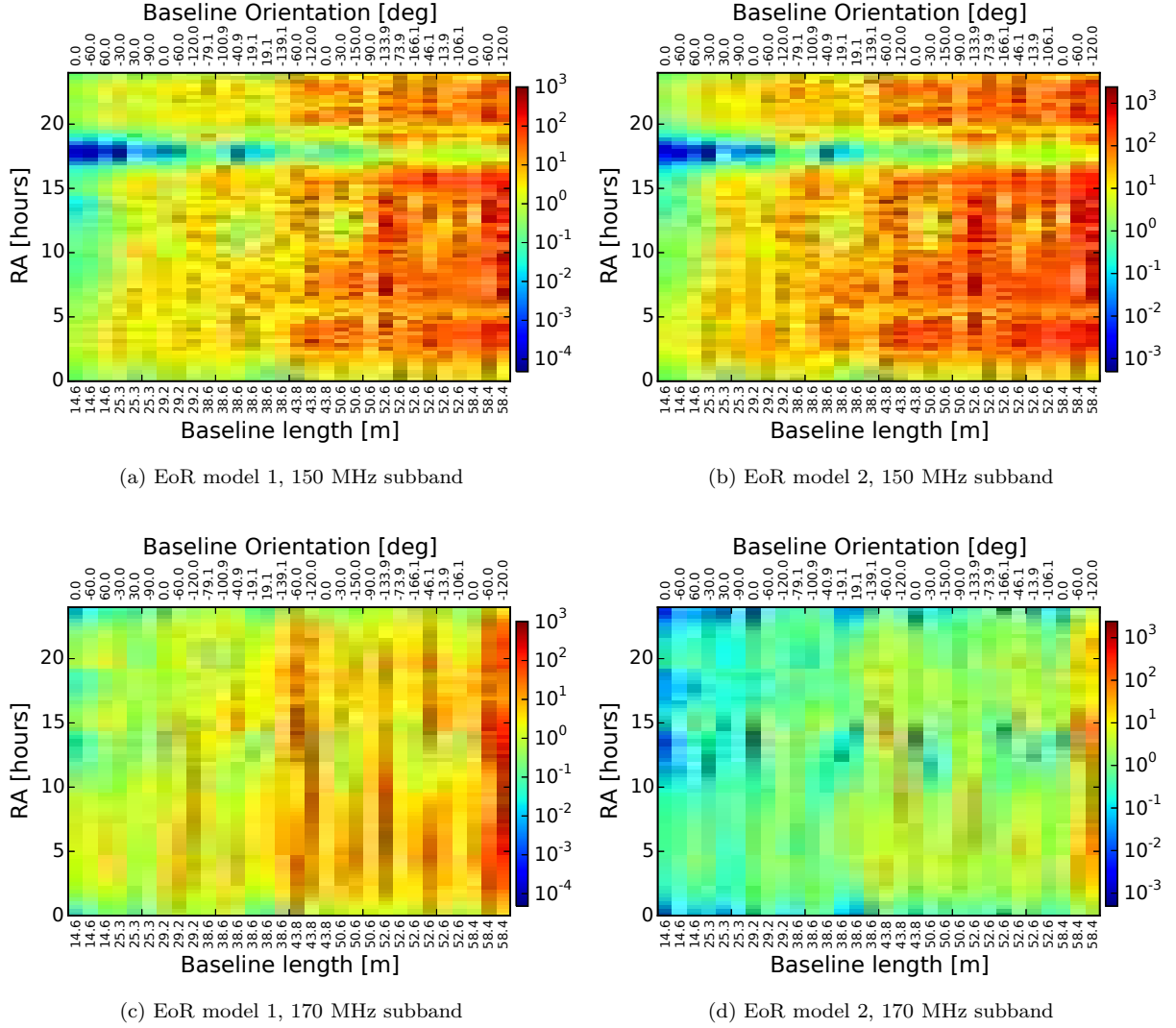
(a) 150 MHz subband ($z \approx 8.47$)(b) 170 MHz subband ($z \approx 7.36$)

Figure 5. EoR signal and foreground delay power spectrum in units of $K^2(h^{-1} \text{ Mpc})^3$ in 150 MHz (top) and 170 MHz (bottom) subbands ($B_{\text{eff}} = 10 \text{ MHz}$) on eight unique baseline lengths of HERA-19 at arbitrary LST. The length and orientation of the baseline vector corresponding to each panel is annotated on the top right corner. EoR models 1 and 2 are shown in cyan and gray respectively. The foregrounds obtained with achromatic, *Airy* and simulated chromatic antenna beams are shown in black, red and blue respectively. EoR detection sensitivity is highest for antenna beam with least chromaticity and vice versa. Even for the simulated chromatic antenna beam pattern, which has the highest chromaticity among the antenna beam models considered, foreground power will be lower than two independent EoR models by more than two orders of magnitude for $|k_{\parallel}| \gtrsim 0.2 h \text{ Mpc}^{-1}$ on all HERA baselines.

**Figure 6.**

- Ali, S. S., Bharadwaj, S., & Chengalur, J. N. 2008, *MNRAS*, 385, 2166
- Beardsley, A. P., Hazelton, B. J., Morales, M. F., et al. 2013, *MNRAS*, 429, L5
- Bernardi, G., de Bruyn, A. G., Brentjens, M. A., et al. 2009, *A&A*, 500, 965
- Bernardi, G., de Bruyn, A. G., Harker, G., et al. 2010, *A&A*, 522, A67
- Bock, D. C.-J., Large, M. I., & Sadler, E. M. 1999, *AJ*, 117, 1578
- Bowman, J. D., Morales, M. F., & Hewitt, J. N. 2009, *ApJ*, 695, 183
- Bowman, J. D., Cairns, I., Kaplan, D. L., et al. 2013, *PASA*, 30, 31
- Condon, J. J., Cotton, W. D., Greisen, E. W., et al. 1998, *AJ*, 115, 1693
- Datta, A., Bowman, J. D., & Carilli, C. L. 2010, *ApJ*, 724, 526
- de Oliveira-Costa, A., Tegmark, M., Gaensler, B. M., et al. 2008, *MNRAS*, 388, 247
- Di Matteo, T., Perna, R., Abel, T., & Rees, M. J. 2002, *ApJ*, 564, 576
- Dillon, J. S., Liu, A., & Tegmark, M. 2013, *Phys. Rev. D*, 87, 043005
- Dillon, J. S., Liu, A., Williams, C. L., et al. 2014, *Phys. Rev. D*, 89, 023002
- Ewall-Wice, A., Bradley, R., DeBoer, D., et al. 2016, *ArXiv e-prints*, arXiv:1602.06277
- Furlanetto, S. R., & Briggs, F. H. 2004, *New A Rev.*, 48, 1039
- Furlanetto, S. R., Oh, S. P., & Briggs, F. H. 2006, *Phys. Rep.*, 433, 181
- Furlanetto, S. R., Zaldarriaga, M., & Hernquist, L. 2004, *ApJ*, 613, 1
- Ghosh, A., Prasad, J., Bharadwaj, S., Ali, S. S., & Chengalur, J. N. 2012, *MNRAS*, 426, 3295
- Gleser, L., Nusser, A., & Benson, A. J. 2008, *MNRAS*, 391, 383
- Harris, F. J. 1978, *IEEE Proceedings*, 66, 51
- Iliev, I. T., Shapiro, P. R., Ferrara, A., & Martel, H. 2002, *ApJ*, 572, L123
- Lidz, A., Zahn, O., McQuinn, M., Zaldarriaga, M., & Hernquist, L. 2008, *ApJ*, 680, 962
- Liu, A., Parsons, A. R., & Trott, C. M. 2014a, *Phys. Rev. D*, 90, 023018
- . 2014b, *Phys. Rev. D*, 90, 023019
- Liu, A., & Tegmark, M. 2011, *Phys. Rev. D*, 83, 103006
- Liu, A., Tegmark, M., Bowman, J., Hewitt, J., & Zaldarriaga, M. 2009, *MNRAS*, 398, 401
- Lonsdale, C. J., Cappallo, R. J., Morales, M. F., et al. 2009, *IEEE Proceedings*, 97, 1497
- Madau, P., Meiksin, A., & Rees, M. J. 1997, *ApJ*, 475, 429
- Mauch, T., Murphy, T., Buttery, H. J., et al. 2003, *MNRAS*, 342, 1117
- McQuinn, M., Zahn, O., Zaldarriaga, M., Hernquist, L., & Furlanetto, S. R. 2006, *ApJ*, 653, 815
- Mesinger, A., Furlanetto, S., & Cen, R. 2011, *MNRAS*, 411, 955

- Morales, M. F., Bowman, J. D., & Hewitt, J. N. 2006, *ApJ*, 648, 767
- Morales, M. F., Hazelton, B., Sullivan, I., & Beardsley, A. 2012, *ApJ*, 752, 137
- Morales, M. F., & Hewitt, J. 2004, *ApJ*, 615, 7
- Neben, A. R., Bradley, R. F., Hewitt, J. N., et al. 2016, *ArXiv e-prints*, arXiv:1602.03887
- Paciga, G., Albert, J. G., Bandura, K., et al. 2013, *MNRAS*, 433, 639
- Parsons, A., Pober, J., McQuinn, M., Jacobs, D., & Aguirre, J. 2012a, *ApJ*, 753, 81
- Parsons, A. R., & Backer, D. C. 2009, *AJ*, 138, 219
- Parsons, A. R., Pober, J. C., Aguirre, J. E., et al. 2012b, *ApJ*, 756, 165
- Parsons, A. R., Backer, D. C., Foster, G. S., et al. 2010, *AJ*, 139, 1468
- Parsons, A. R., Liu, A., Aguirre, J. E., et al. 2014, *ApJ*, 788, 106
- Pober, J. C., Parsons, A. R., Aguirre, J. E., et al. 2013, *ApJ*, 768, L36
- Santos, M. G., Cooray, A., & Knox, L. 2005, *ApJ*, 625, 575
- Scott, D., & Rees, M. J. 1990, *MNRAS*, 247, 510
- Sunyaev, R. A., & Zeldovich, Y. B. 1972, *A&A*, 20, 189
- Taylor, G. B., Carilli, C. L., & Perley, R. A., eds. 1999, *Astronomical Society of the Pacific Conference Series*, Vol. 180, *Synthesis Imaging in Radio Astronomy II*
- Thompson, A. R., Moran, J. M., & Swenson, Jr., G. W. 2001, *Interferometry and Synthesis in Radio Astronomy*, 2nd Edition (Wiley)
- Thyagarajan, N., Udaya Shankar, N., Subrahmanyan, R., et al. 2013, *ApJ*, 776, 6
- Thyagarajan, N., Jacobs, D. C., Bowman, J. D., et al. 2015a, *ApJ*, 807, L28
- . 2015b, *ApJ*, 804, 14
- Tingay, S. J., Goeke, R., Bowman, J. D., et al. 2013, *PASA*, 30, 7
- Tozzi, P., Madau, P., Meiksin, A., & Rees, M. J. 2000, *ApJ*, 528, 597
- Trott, C. M., Wayth, R. B., & Tingay, S. J. 2012, *ApJ*, 757, 101
- van Cittert, P. H. 1934, *Physica*, 1, 201
- van Haarlem, M. P., Wise, M. W., Gunst, A. W., et al. 2013, *A&A*, 556, A2
- Vedantham, H., Udaya Shankar, N., & Subrahmanyan, R. 2012, *ApJ*, 745, 176
- Wang, X., Tegmark, M., Santos, M. G., & Knox, L. 2006, *ApJ*, 650, 529
- Zaldarriaga, M., Furlanetto, S. R., & Hernquist, L. 2004, *ApJ*, 608, 622
- Zernike, F. 1938, *Physica*, 5, 785